RSC Advances

ROYAL SOCIETY OF CHEMISTRY

www.rsc.org/advances

ARTICLE TYPE www. rsc.org/xxxxxx | XXXXXXXX

Mechanical stability of Zinc Oxide nanowires under tensile loading: Is wurtzite stable at the nanoscale?†

Germán J. Soldano,‡* Franco M. Zanotto,‡ and Marcelo M. Mariscal*

Received Xth XXXXXXXXXX 20XX, Accepted Xth XXXXXXXXX 20XX
First published on the web Xth XXXXXXXXXX 200X
DOI: 10.1039/b000000x

The mechanical response of zinc oxide nanowires under uniaxial tensile loading is investigated by molecular dynamics and supported by density functional calculations. Previous theoretical works predict a stress-induced phase transition which has not been observed experimentally in zinc oxide nanowires up to date. Here, we report an explanation for such a discrepancy. Our simulations reveal brittle failure at room temperature without phase transformation, in agreement with experiments. Interestingly, we also find that if temperature is raised to 600 K, the phase transition occurs. A detailed reaction mechanism is proposed. For the first time, the associated constant rate has been calculated. Based on these results we propose an experimental procedure to finally observe the predicted phase transformation.

1 Introduction

Zinc oxide (ZnO) stands out as one of the most versatile nanomaterials. The technological applications of this wide-band-gap semiconductor are vast and diverse, among which we can mention: solar cell window layers, catalysis, gas and chemical sensors, optical and electrical devices, cosmetics etc.[1–3] One of its most promising features is piezoelectricity, i.e., its potential of converting mechanical energy into electricity.[4] The voltage induced by mechanical stress is proportional to the maximum achievable strain. Since one-dimensional (1-D) ZnO structures can stand 5 times more strain than the bulk material, ZnO nanowires (NWs) are the ideal system to use in piezoelectric nanodevices.[5] Synthesis, characterization, and applications of 1-D ZnO nanostructures are given in ref,[2] we avoid replications here.

In order to benefit the development of such ZnO devices, a deeper understanding of its mechanical properties in the nanoscale is essential.[4,6] Due to the great advance in computational power, Molecular Dynamics (MD) simulations and Density Functional Theory (DFT) calculations appear as excellent tools to fulfill this purpose.

Next, results obtained from previous MD simulations are briefly summarized. Wang et al. were the first to predict that around a strain of 10% at 300 K, ZnO NWs of up to 5 nm in diameter experience a phase transition from wurtzite (WZ, the most stable ZnO bulk structure) to a body-centered-tetragonal (BCT) structure.[7] Later works found that the features of transition are size dependent, particularly for the maximal stress before transformation to BCT.[8–10] Similar results were obtained for NWs with three different cross-sectional shapes,[11] and nanobelts.[9,12] MD simulations on larger NWs (up to 10 nm) suggest that surface defects can significantly lower the strain of transition from 6.7% (pristine NW) to 5.5%.[5] Difference in the fracture strain (6.7% vs 10%[7]) can be ascribed to the different approach for long-range interactions. Simulations agree that brittle failure occurs after phase transition, at a strain of around 17%.

The BCT phase was later confirmed experimentally on ZnO($10\bar{1}0$) surface reconstructions.[13] However, it has not been observed so far on ZnO NWs. In contrast to simulations, experiments revealed brittle fracture at much lower strains (as high as 6.2%) without any signs of phase transition.[5] It is very important to notice, however, that all the simulation studies described above were performed with the Buckingham potential.[14,15] This is a non-reactive pairwise potential, therefore quantitative aspects regarding bond breaking and bond formations should be taken with care. Specially for phase transformations, where such bond processes are crucial, the Buckingham potential can only qualitatively describe the phenomenon.

DFT calculations, on the other hand, found that the WZ-BCT transition occurs prior to fracture at 20% strain,[16] at least twice the value predicted by the Buckingham potential. Still, DFT studies were performed as molecular mechanics simulations at 0 K so that the effect of atomic motion and temperature were not considered.[3,16,17] Also, the dimensions of the systems studied were very small due to the computational cost. These drawbacks prevent DFT studies to describe brittle

† Electronic Supplementary Information (ESI) available: videos and figures are available. See DOI: 10.1039/b000000x/

INFIQC - Departamento de Matemática y Física - Facultad de Ciencias Químicas Universidad Nacional de Córdoba, Argentina. Fax: +49 731 50 22819; Tel: +49 731 50 31340; E-mail: marcelo.mariscal@conicet.gov.ar, gersoldano@gmail.com

‡ These authors contributed equally to this work.

fractures and/or phase transitions realistically.

In summary, the Buckingham potential fails to describe quantitative aspects of the WZ-BCT transition, and DFT cannot give insights into the effect of temperature on the mechanical properties of ZnO NWs.

Here, we report a systematic study of the mechanical response of ZnO NWs under tensile loading using a state-of-the-art reactive potential. This reactive force field (ReaxFF) accounts for bond breaking and bond formation processes. In order to test its performance, DFT calculations on 1-D nanostructures were also carried out. An excellent agreement between ReaxFF and DFT was found. Our MD simulations reveal that under tensile loading at 300 K, ZnO NWs do not experience phase transition but brittle failure, in perfect agreement with experiments. Interestingly, the transition does occur if the temperature is raised to 600 K. Through this article, we proposed a detailed mechanism of the WZ-BCT transition in NWs, and estimate its rate constant as a function of temperature and strain. To the best of our knowledge, this has not been addressed before. Finally, we proposed an experimental procedure to observe such a fascinating phenomenon.

2 Computational Details

Ab initio calculations were performed using the Quantum Espresso/PWSCF code[18]. Vanderbilt ultrasoft pseudopotentials[19] were used with the Perdew-Burke-Ernzerhof[20] (PBE) and the local density approximation[21] (LDA). A 490 eV (36 Ry) kinetic energy cutoff and a 4082 eV (300 Ry) charge density cutoff was used. The reciprocal space was sampled with a (8×8×5) and a (1×1×6) k-point grid for NWs and nanotubes (NTs), respectively. Both grids were generated automatically using the Monkhorst–Pack method[22]. All these inputs were carefully parameterized. A Gaussian broadening of 0.136 eV (0.01 Ry) was applied. The convergence of the forces for DFT relaxations are equal to 0.02 eV/Å. The unit cells consisted of NWs and NTs of two bilayers separated 8.4 Å from their lateral periodic images. A video showing a NW and a NT is provided in the supporting information (SI), and explained in Fig. s1.

Energy minimizations and molecular dynamics simulations (MD) were carried out using the Large-scale Atomic-Molecular Massively Parallel Simulator[23] (LAMMPS). The zinc-oxygen interactions were described with the reactive force field ReaxFF,[24,25] as it is implemented in the LAMMPS subroutine.[26] Simulations were performed with a constant number of atoms and constant temperature using the Nose-Hoover thermostat, with a time step of 1 fs. Unless otherwise mentioned, all NWs in this work are $[0001]$ oriented wurtzite structures with hexagonal cross-section exposing the $\{10\bar{1}0\}$ facets. For MD simulations, seven ZnO bilayers were used to account for the possible surface reconstructions. Periodic boundary conditions were implemented for the three dimensions, keeping NWs separated by at least 20 Å with respect to their periodic images. Initial velocities were randomly assigned following a Maxwell-Boltzmann distribution. The length of the simulation box along the wire axis was increased at 0.2 m/s, simulating tensile loading. Slower stretchings did not affect the results. Tensile stress was obtained as the sum of the z component of the stress tensor of each atom, as calculated by the *compute_stress_atom* subroutine included in LAMMPS.

Nudged elastic band (NEB) calculations were performed following the discussion of Ref.[27–29] as implemented in LAMMPS, using 32 images between metastable states. The associated activation energy was converged with three supercells (see Fig. s7).

3 Results and Discussion

3.1 ReaxFF performance on nanostructures

Originally, a ReaxFF for zinc and oxygen was parametrized for bulk and surface structures using the B3LYP-functional.[24,25] Good agreement with DFT calculations was observed. Here, we extended the testing to nanostructures such as NWs and NTs, using the most commonly implemented DFT functionals: GGA and LDA. Since some differences could arise from the different quantum mechanical approaches, bulk and surface properties were calculated as well. Table 1 shows ZnO bulk parameters and energies according to experiments, GGA, LDA, and ReaxFF. Our

Table 1 Measured and calculated lattice constants (a,b,c), cohesive energy of ZnO wurtzite per zinc-oxygen pair (E_WZ), cohesive energy difference per pair between rocksite and wurtzite (ΔE_{RS-WZ}), and between zinc-blende and wurtzite structures (ΔE_{ZB-WZ})

	experiment	GGA	LDA	ReaxFF
a,b (Å)	3.250[30]	3.287	3.185	3.282
c (Å)	5.207[30]	5.303	5.152	5.305
E_WZ (eV)	7.56[31]	7.28	8.98	7.76
ΔE_{RS-WZ} (eV)	–	0.292	0.221	0.402
ΔE_{ZB-WZ} (eV)	–	0.014	0.013	0.021

DFT results are in good agreement with measured values and coincide with previous theoretical works.[1,32–36] As usual, LDA overestimates the cohesive energy, however, it correctly estimates the energetic difference between structures. The accordance between the force field and our ab initio calculations is as good as in the original works.

Next, the force field performance on 1-D structures was evaluated. Several ZnO NWs and NTs of different diameters were relaxed using both, DFT and ReaxFF. An example

of each structure is depicted in Fig1a (a complete set of geometries is provided in Fig. s3). Their stability was quantified through the formation energy, according to

$$E_f = E_{1D}(\mathrm{m})/m - E_{bulk} \quad (1)$$

where $E_{1D}(\mathrm{m})$ is the energy of a NW or NT with m ZnO pairs, and E_{bulk} is the energy of the wurtzite bulk per pair. As can be observed in Fig. 1b, DFT and ReaxFF curves show the same trends. Our DFT results using GGA are in perfect agreement

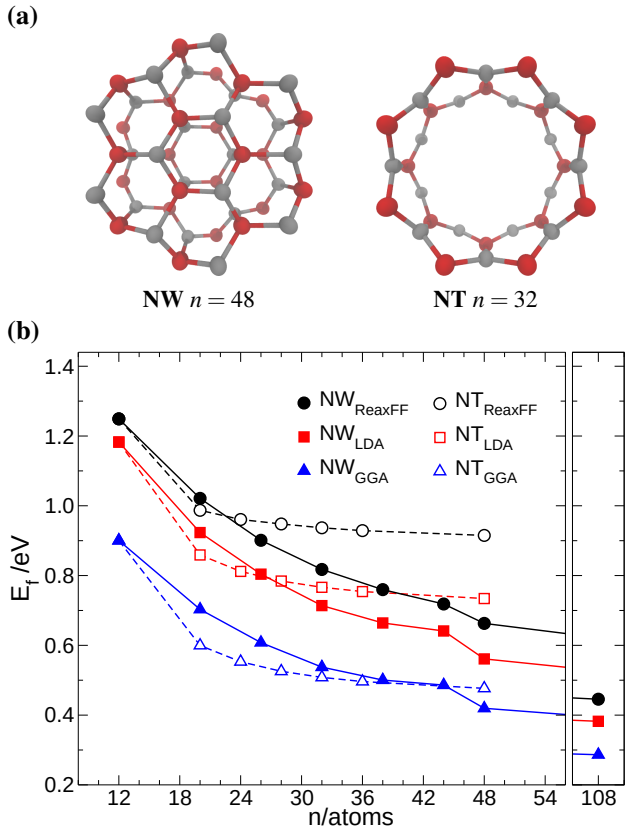

Fig. 1 (a) Unit cell cross sections for a NW and a NT with 48 and 32 atoms, respectively. (b) Formation energy E_f of several NWs and NTs after relaxation according to GGA, LDA, and ReaxFF (bottom). Points have been connected with lines in order to ease the comparison.

with the work of Shen et al.[33] who predicted that ZnO NTs are more stable than ZnO NWs below a crossover point near 38 atoms. According to LDA results, the crossover occurs at around 26 atoms, which is very close to the force field prediction (at around 23 atoms).

These results provide solid evidence that ReaxFF is a very reliable and suitable tool to study ZnO 1-D nanostructures. Its reproducibility and agreement with DFT calculations is remarkable, allowing us to confidently explore the mechanical properties of ZnO NWs.

3.2 Mechanical stability

In this section, the response of ZnO NWs against axial loading is studied. MD simulations were carried out on five [0001] oriented hexagonal NWs of different diameters (detailed in Table 2) at three different temperatures: 100, 300, and 600 K. In order to choose the surface facet, we focused on

Table 2 Diameter (d) and number of atoms (n) per unit cell for the NWs selected to perform molecular dynamics. Top views are also shown

	NW_I	NW_{II}	NW_{III}	NW_{IV}	NW_V
d[Å]	9.6	16.8	23.2	29.4	36.2
n	336	756	1344	2100	3024
top view	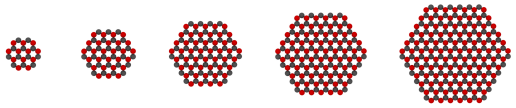				

the two most commonly observed in X-ray diffraction[37] and high-resolution scanning tunneling microscopy[38]: $[10\bar{1}0]$ and $[11\bar{2}0]$. After a careful study of the surface stability (shown in Fig. s4-s5 and text in the SI) the $[10\bar{1}0]$ facet was chosen for further calculations for being the most stable.

Fig. 2 shows tensile stress as a function of axial strain. As NWs are stretched, the bond distance increases, and so does the force that attempts to counteract the process. This causes the stress to increase almost linearly with the strain, typical features of an elastic deformation. This implies that a complete recoverability from strain is achieved if the stress is removed. Below 600 K, stress eventually becomes so high, that the structure can not longer hold, leading to brittle fracture and the formation of an amorphous neck. Within the neck, the load is relieved by local relaxations while, far from it, the atoms return to their crystalline equilibrium positions. Consequently, the tensile stress jumps abruptly to lower values (see breaks at 100 and 300 K in Fig. 2). These are typical features of plastic deformations. In agreement with previous work, simulations at 100 and 300 K show that the response of uniaxial loading is size dependent.[8–10] However, the differences are relatively small. The strain of brittle fracture is actually more sensitive to the temperature, decreasing from 20% at 100 K, to 13% at 300 K.

In contrast to all previous MD studies, our simulations show that the WZ-BCT transition does not occur at 300 K, instead brittle failure is observed. This is in perfect agreement with the experimental finding.[5] Interestingly, the transformation does occur at 600 K, as it is evident from Fig. 2 (bottom panel). A clear size-dependent behavior is found for the strain of phase transition, the latter being higher for wider NWs. The resulting BCT structure is sufficiently stable to endure further stretchings, up to a 20% strain. These results indicate

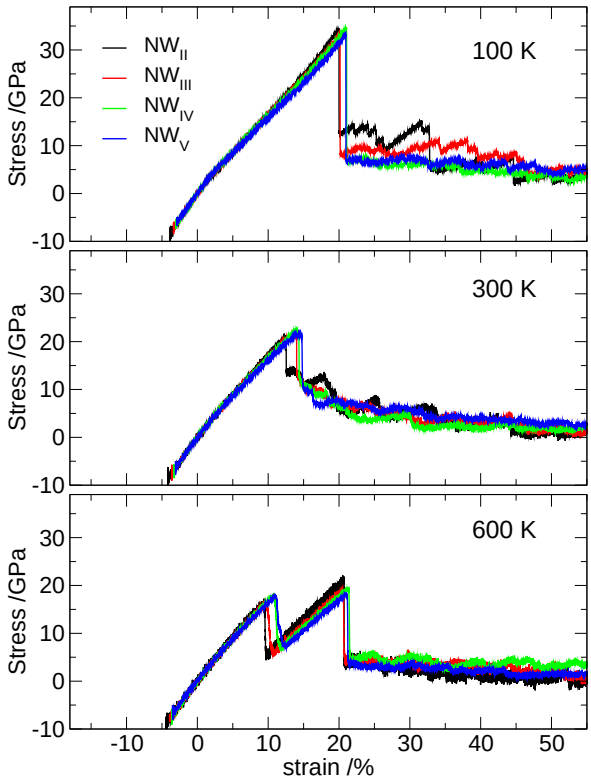

Fig. 2 Tensile stress as a function of the strain for the chosen nanowires at 100, 300, and 600 K.

that temperature is playing a key role in the process. Details regarding the phase transition are given in section 3.4.

In order to quantify the stiffness of these materials the Young's modulus (Y) was calculated, shown in Table 3. A NW with a large value of Y is relatively unstretchable, i.e., a large stress is required for a given strain. Values of Y are in the order of 170 GPa, which is one order of magnitude greater than in ductile materials (gold NWs, $Y \approx 60$ GPa[39]), one order of magnitude lower than in rigid materials (carbon NTs, $Y \approx 1800$ GPa[40]), and about the same order but higher than in ZnO wurtzite bulk ($Y \approx 144$ GPa).

Table 3 Young's moduli Y of NWs from MD at 300 K

	NW_I	NW_{II}	NW_{III}	NW_{IV}	NW_V
Y [GPa] WZ	213	177	172	170	163
Y [GPa] BCT	187	142	135	131	128

The Young's modulus was found to decrease with the increase of the NW diameter, in agreement with previous simulations.[8,9] This behavior has been ascribed to the high radial concentration of atoms, which in turns is due to surface compression.[41] Remarkably, surface compression is also responsible for the opposite effect, i.e., the increase of Y with the increase of the NW diameter.[6] Due to the Poisson effect,[42] radial compression induces longitudinal elongations of NWs, which in turns decreases the Young's modulus. Since this so-called intrinsic strain decreases as the NWs get wider, Y increases. Briefly, Y first decreases with the diameter increase due to the high radial concentration of atoms, and then increases to the bulk value due to the decrease of the longitudinal elongation. This behavior has been experimentally observed in cobalt NWs wider than 70 nm.[6] Although simulating NWs of such dimensions is beyond our computer capacity, we found convincing evidence of the intrinsic strain. The equilibrium lattice parameter "c" of ZnO was found to decrease with the increase of the NW diameter (see Fig. s6).

Although reported experimental values change from one work to the other (from 20-58 GPa[43–50] to 100-200 GPa.[41,51–55]) all of them agree that the Young's modulus decreases with the NW diameter,[8,9] which is in line with the theoretical outcome.

Table 3 also shows the Young's modulus of NWs in the BCT phase. The same trend of Y with respect to the diameter is found, although in this case, values are around $\sim$20% lower than that of the WZ phase. Results for NW_I, the thinnest of the set, follow the same trends described in this section.

3.3 Structural and thermodynamic aspects

The equilibrium structures at zero strain for NW_{II} in WZ and BCT phases are provided in Fig. 3 The most noticeable aspect of the BCT structure is the presence of concentrically

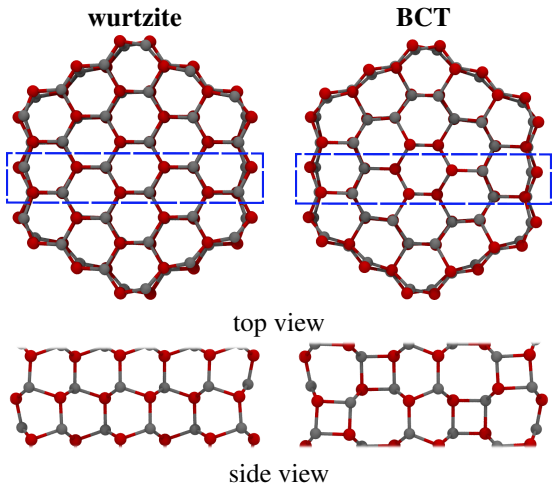

Fig. 3 Top view of wurtzite and body-centered-tetragonal structures of NW_{II}. The side view is restricted to the atoms inside the blue dashed rectangle shown in the top view.

aligned squares (formed by four neighboring atoms), i.e., all the square planes intersect at the NW central axis. This is significantly different from the BCT bulk structure, where the square planes are all parallel to each other.[7] Just like in the wurtzite case, in the BCT structure, every atom has four first neighbors. However, one of the tetrahedral angles is more acute (around 91°), which is one of the square vertex. These structural differences manifest in the vibrational density of states (VDOS), where WZ and BCT phases can be easily distinguished (see details and Fig. s7 in the SI).

Valuable information can be obtained from the equilibrium energy of WZ and BCT NWs as a function of strain. With this purpose, NWs in both structures were fully relaxed at several fixed lengths (along the c-axis) using ReaxFF and DFT. To facilitate the comparison, energies and strains are referred to that of the corresponding WZ NW at equilibrium and zero strain. As deduced from Fig. 4a, ab initio calculations verifies that BCT NWs are stable structures. In fact, they show that for NW_I the BCT phase is even more stable than the WZ phase (if their equilibrium energies are compared). This is also the case of NW_{II} according to GGA results. A similar analysis was made for both phases in the bulk material,[7] in which it was found that the BCT phase becomes the most stable at stresses higher than 7 GPa.

A crucial feature to study, is the crossover point, i.e., the point at which the curves of both structures intersect in Fig. 4a. The strain of crossover indicates the strain at which the BCT phase becomes more stable than wurtzite phase. As the diameter increases (from NW_I to NW_{II}), the crossover shifts to greater strains and higher energies. ReaxFF slightly underestimates the relative stability of BCT NWs. Indeed, the relative energy difference between ReaxFF and LDA is of the same order than that between the two DFT techniques studied. Moreover, the tendency of the crossover to shift to higher strains and energies with the NW diameter is correctly captured by the force field. This allows us to explore larger systems using ReaxFF.

It is instructive to study how fast the crossover shifts with the NW size. If at a certain diameter the crossover occurs at a large strain value (25%, for instance) it is very unlikely that the phase transition take place since at that strain the wire suffers brittle failure even at very low temperatures. With this motivation, the crossover point was calculated using ReaxFF for several NWs with diameters from 9 Å to almost 50 Å. As shown in Fig. 4b, the crossover strain as a function of the diameter converges asymptotically to a strain of ∼8%, which is safely below the strain of brittle failure (Fig. 2). This implies that the WZ-BCT transition could also occur in NWs wider than 5 nm under tensile loading. More so, the converged value of crossover strain may be even lower considering that the force field underestimates the stability of BCT NWs.

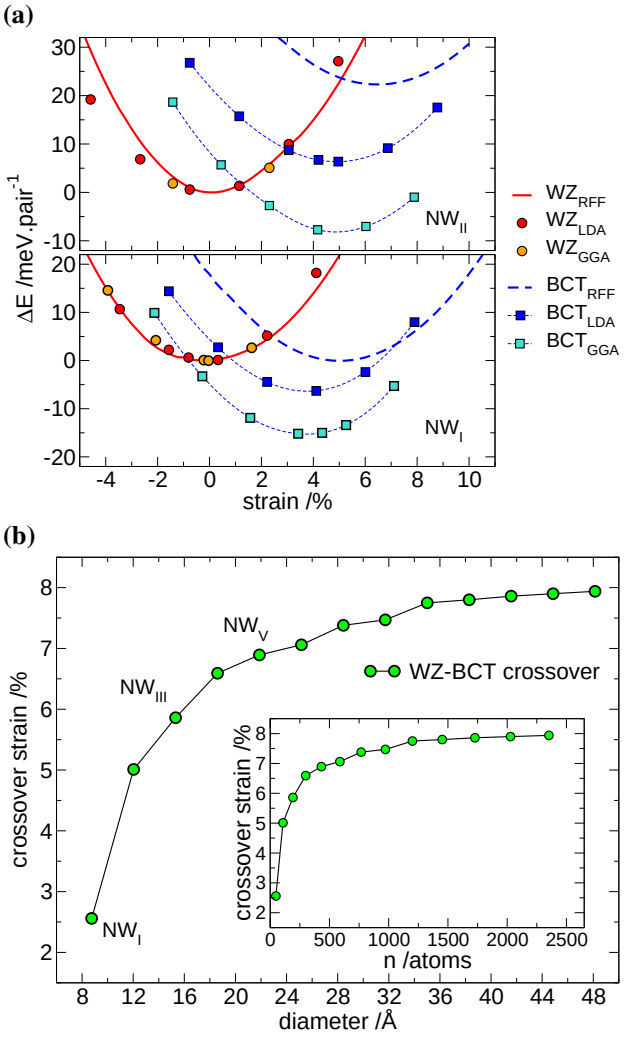

Fig. 4 (a) Energy per ZnO pair of WZ and BCT nanowires as a function of the strain according to the force field (RFF) and DFT (LDA and GGA). For each method, energy and strain are referred to that of the corresponding wurtzite NW in equilibrium. The strain at which the RFF curves intersect is the crossover strain. Only points are shown WZ_{LDA} and WZ_{GGA} values to avoid confusion. (b) Strain of the crossover as a function of the NW diameter, according to ReaxFF. The inset shows this dependence with the number of atoms per unit cell.

3.4 Phase transition mechanism

Results so far indicate that at certain strains, the BCT structure is thermodynamically favored over the WZ structure. However, this is not sufficient to claim that the former should exist in nature: a kinetic insight is required. Indeed, simulations suggest that the process is kinetically hindered (Fig. 2). In order to finally predict its feasibility, the mechanism of the WZ-BCT transformation was investigated. Previous simulations

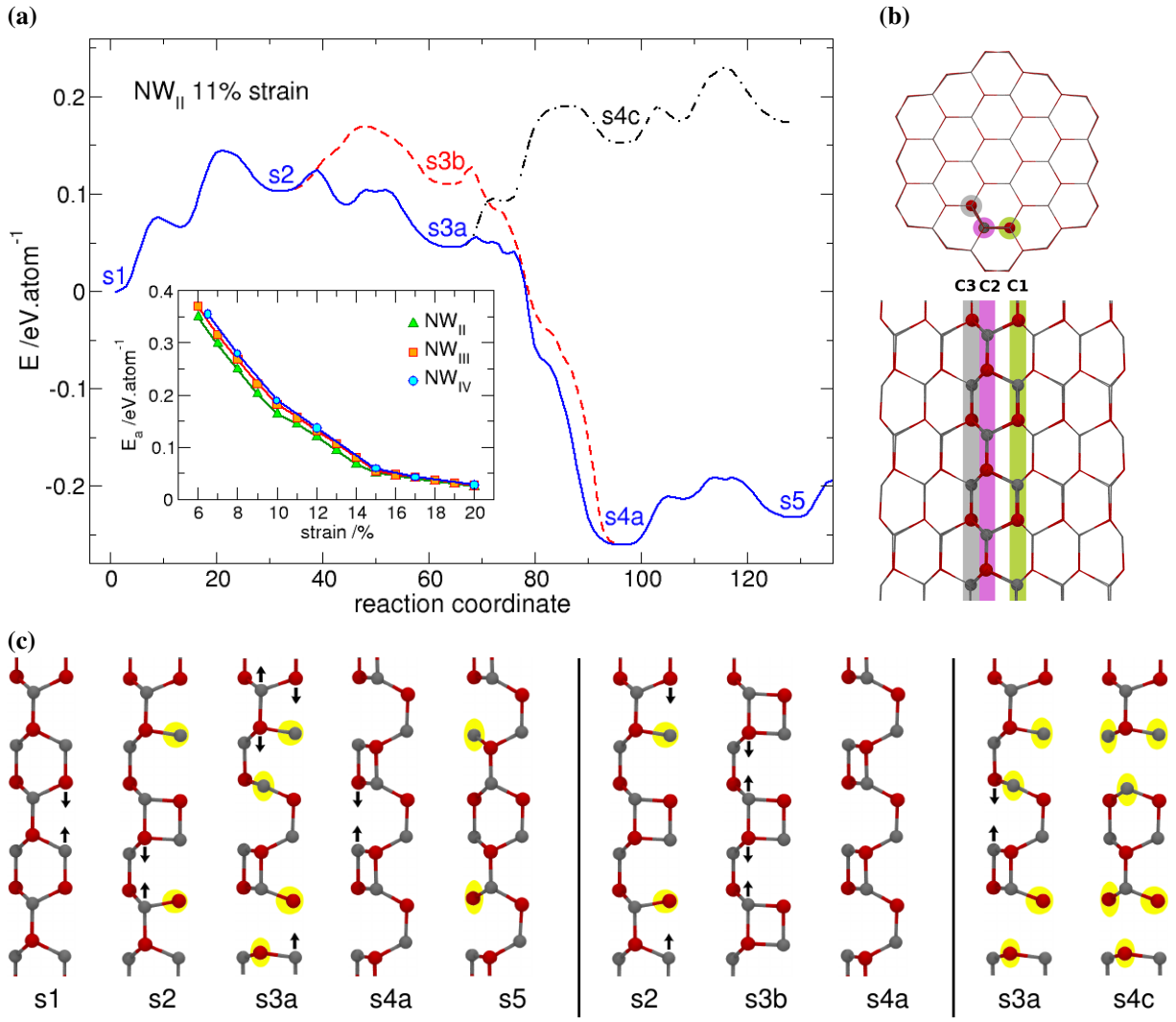

Fig. 5 (a) Reaction coordinate for three pathways of the wurtzite-BCT transformation for NW_{II} at 11% of strain. Only the first steps of the mechanism are shown (the full reaction cascade is shown in the supplementary information). The pathway with the lowest activation energy is colored blue. The inset shows the activation energy associated with the latter pathway as a function of the strain for NW_{II}, NW_{III}, and NW_{IV}. (b) Top and side views of NW_{II} in the wurtzite structure. Atoms that experience bond breaking or bond formation are depicted as red (oxygen) and gray (zinc) spheres. Three atom columns are highlighted as C1-C3. (c) Relocation of the atoms along the reaction pathways. For the sake of clarity, only the highlighted atoms (Fig. 5b) are shown. Three-coordinated atoms are remarked by a yellow ellipse.

already found that the stress-induced WZ-BCT phase transition originates from the surface and radially spreads toward the NW core.[5] We have found the same trend for NWs of different diameters and at different temperatures. We also found that the process occurs through metastable steps, involving the bond breaking and bond formation of atoms along strings aligned to the c-axis. Later, neighboring strings undergo the same process. In the following, such strings will be referred as columns, highlighted in Fig. 5b (C1-C3). NW_{II} at 11% of strain is chosen as an illustrative example. Three reaction pathways were proposed, depicted in Fig. 5c. For clarity, only C1-C3 columns are shown instead of the whole NW.

The first reaction pathway was inspired by MD simulations, in which it was observed that the bond reorganization takes place first in two vicinal columns, and only then continues in a third one (s1-s2-s3a-s4a-s5 in Fig. 5c). In the second path, the bond breaking/formation is completed in one column, before continuing in the second one (s1-s2-s3b-s4a in Fig. 5c). Finally, in the third path, the phase transition starts in one column and spreads in neighboring columns before completing

the process in the first one (s1-s2-s3a-s4c in Fig. 5c).

The associated activation energies are shown in Fig. 5a. In general, the instability of the stages increases with the number of unsaturated atoms (highlighted in yellow in Fig. 5c). This immediately discards the third pathway. The first two paths are close in energy, but the second implies greater angle distortions, making it energetically unstable with respect to the first one. In conclusion, the first pathway is the one with the lowest activation energy.

At the end of this path, columns C1 and C2 have acquired the BCT structure. In order for the phase transition to be completed, this process has to be repeated several times. In each cycle, a new column pair transforms from WZ to BCT, from the surface to the NW core, as explained above.

NEB calculations associated with the entire process show that the phase transition occurs in a cascade fashion: From stage 4a on, the reaction proceeds energetically downhill (see Fig. s8). Therefore, the transformation of columns C1 and C2 is the rate-determining step of the WZ-BCT conversion. The same behavior was observed at different strains and NW diameters.

Since the energy required for bond breaking declines as the bonds get longer, the uniaxial tensile loading should decrease the activation energy. This is confirmed in the inset of Fig. 5a, where the activation energy for the phase transition (E_a) as a function of the strain is shown for three NWs. The three curves follow very similar trends, with slightly higher values for wider NWs. This is in agreement with the increase of the phase transition strain with the increase of the NW diameter (Fig. 2, bottom panel).

Using the Arrhenius formula it is possible to estimate the rate constant of the WZ-BCT transformation:

$$k_t = A \exp\left(\frac{-E_a(strain)}{kT}\right) \qquad (2)$$

where A is the pre-exponential factor, E_a the activation energy, k the Boltzmann constant, and T the temperature. Fig. 6 shows the rate constant dependence with temperature and strain for NW_{II}, assuming a pre-exponential factor $A = 10^{13}\ s^{-1}$. For the sake of clarity, these results are shown in two plots, at low and high temperatures. Strain is restricted to values higher or equal than that of the WZ-BCT crossover (Fig. 4b); below these values the phase transition becomes infeasible. Rate constant values for high temperatures are in perfect agreement with our MD simulations. They both predict that at 10% of strain and 600 K the phase transition should occur in few picoseconds. Fig. 6 also reveals that the WZ-BCT transformation can occur at lower temperatures but at prohibited times for MD simulations (due to the computational cost).

As observed in Fig. 2, brittle failure can occur instead of phase transition. These cases are highlighted as green regions in the rate diagrams of Fig. 6. Outside them, thermal motion of

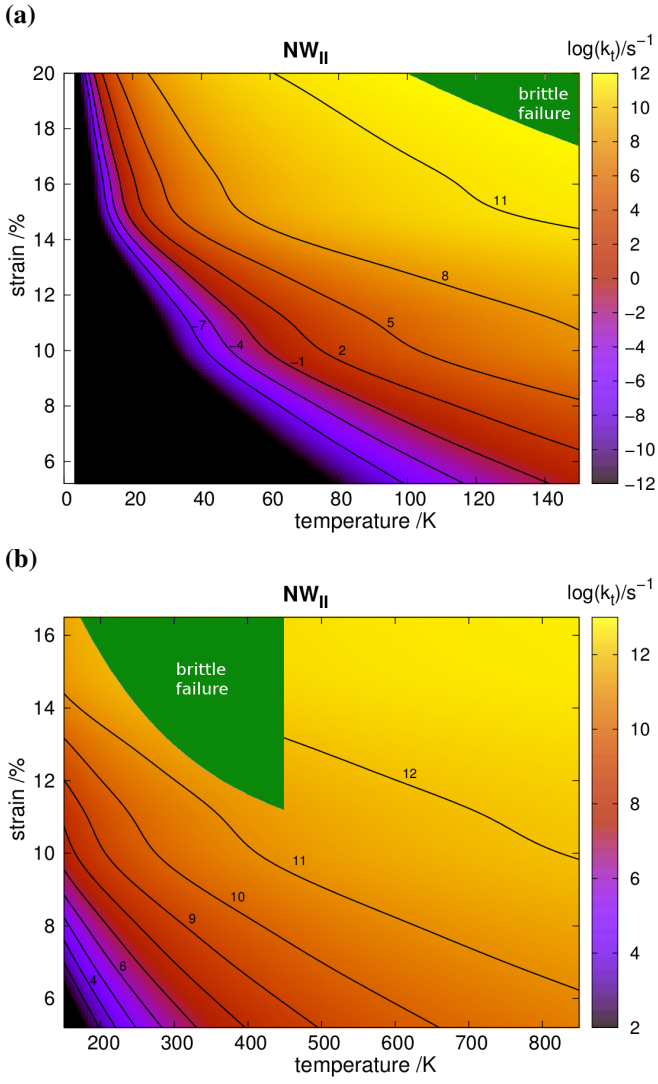

Fig. 6 Logarithm of the rate constant for the WZ-BCT transition ($\log_{10}[k_t]$) as a function of the temperature and the strain. Diagram regions in which brittle fracture was observed instead of phase transition (according to MDs) are highlighted in green. Values of some contour lines are labeled to ease the analysis. (a) Low temperatures. (b) High temperatures.

atoms is sufficient to reach the activation energy so that phase transition occurs before brittle fracture.

On the basis of the results exposed in this work, we suggest that experiments should attempt to reach high strains (like 6% as in ref.[5]) but also high temperatures in order to observe the WZ-BCT transition. According to Fig. 2, at a strain of 6% increasing from room temperature to 600 K increases the rate constant of transition by almost four orders of magnitude.

The rate constant dependence with the temperature is of paramount importance for the practical scope of solar cells.

For instance, the solar panels of spacecrafts in the inner solar system must support temperatures from 116 K in the shadow to 424 K in the sun-facing side.[56] Results obtained here can be used as a guideline to promote or prevent the structural transformation on such ZnO based devices. For the first case, Fig. 6 shows strains and temperatures optimal for a fast and safe transition (far from brittle failure). The simplest strategy to avoid the transformation is to keep the tensile loading below 5 % of strain or higher, depending on the nanowire diameter (Fig. 4b).

4 Conclusions

The response of zinc oxide nanowires under tensile loading was investigated by ab initio and reactive force field calculations. In agreement with the experimental observation, our simulations show that wurtzite nanowires at 300 K do not undergo phase transition to the body-centered-tetragonal structure, but brittle failure. Previous MD studies based on the Buckingham potential failed in this prediction. However, we found that the transformation does occur if the loading takes place at 600 K. The trends observed in nanowires of up to 5 nm in diameter suggest that this transition can occur also in wider nanowires. The reaction mechanism involves bond rearrangements of two neighboring strings along the c-axis, which later spreads from the surface to the NW core. The associated rate constant was found to be strongly dependent on the temperature and the nanowire strain. We believe that it may be used as a guidance for future experimental investigations.

Acknowledgments

This work was supported by CONICET PIP 11220110100992, Universidad Nacional de Córdoba, and ANPCyT Program BID (PICT 2010-1233). The authors thank the Texas Advanced Computer Center (TACC) for access to the Stampede supercomputer. Thanks also to the High Performance Computational Center (UNC, Córdoba, Argentina) for access to the Cristina supercomputer. F.M.Z. thanks CIN for the fellowship granted.

References

1 H. Morkoç and U. Özgür, in *General Properties of ZnO*, Wiley-VCH Verlag GmbH and Co. KGaA, 2009, pp. 1–76.
2 Y. Zhang, M. K. Ram, E. K. Stefanakos and D. Y. Goswami, *J. Nanomaterials*, 2012, **2012**, 20:1–20:22.
3 S. Xu and Z. Wang, *Nano Research*, 2011, **4**, 1013–1098.
4 Z. L. Wang and J. Song, *Science*, 2006, **312**, 242–246.
5 R. Agrawal, B. Peng and H. D. Espinosa, *Nano Letters*, 2009, **9**, 4177–4183.
6 X. Huang, G. Li, L. B. Kong, Y. Z. Huang and T. Wu, *Nanoscale*, 2013, **5**, 11643–11648.
7 J. Wang, A. Kulkarni, K. Sarasamak, S. Limpijumnong, F. Ke and M. Zhou, *Phys. Rev. B*, 2007, **76**, 172103.
8 J. Wang, P. Xiao, M. Zhou, Z. R. Wang and F. J. Ke, *Journal of Applied Physics*, 2010, **107**, –.
9 K. Momeni and H. Attariani, *Phys. Chem. Chem. Phys.*, 2014, **16**, 4522–4527.
10 J. He, S. Nagao, J. Wu and Z. Zhang, 2011.
11 W. Lee, J. Chang, S. Ju, M. Weng and C. Lee, *Nanoscale Research Letters*, 2011, **6**, 352.
12 Z.-H. Hong, T.-H. Fang and S.-F. Hwang, *Computational Materials Science*, 2011, **50**, 1944 – 1950.
13 M.-R. He, R. Yu and J. Zhu, *Angewandte Chemie International Edition*, 2012, **51**, 7744–7747.
14 D. J. Binks and R. W. Grimes, *Journal of the American Ceramic Society*, 1993, **76**, 2370–2372.
15 A. J. Kulkarni, M. Zhou and F. J. Ke, *Nanotechnology*, 2005, **16**, 2749.
16 R. Agrawal, J. T. Paci and H. D. Espinosa, *Nano Letters*, 2010, **10**, 3432–3438.
17 M. J. Spencer, *Progress in Materials Science*, 2012, **57**, 437 – 486.
18 P. Giannozzi, S. Baroni, N. Bonini, M. Calandra, R. Car, C. Cavazzoni, D. Ceresoli, G. L. Chiarotti, M. Cococcioni, I. Dabo, A. Dal Corso, S. de Gironcoli, S. Fabris, G. Fratesi, R. Gebauer, U. Gerstmann, C. Gougoussis, A. Kokalj, M. Lazzeri, L. Martin-Samos, N. Marzari, F. Mauri, R. Mazzarello, S. Paolini, A. Pasquarello, L. Paulatto, C. Sbraccia, S. Scandolo, G. Sclauzero, A. P. Seitsonen, A. Smogunov, P. Umari and R. M. Wentzcovitch, *Journal of Physics: Condensed Matter*, 2009, **21**, 395502 (19pp).
19 D. Vanderbilt, *Phys. Rev. B*, 1990, **41**, 7892–7895.
20 J. P. Perdew, K. Burke and M. Ernzerhof, *Phys. Rev. Lett.*, 1996, **77**, 3865–3868.
21 S. H. Vosko, L. Wilk and M. Nusair, *Canadian Journal of Physics*, 1980, **58**, 1200–1211.
22 J. H. Monkhorst and D. J. Pack, *Phys. Rev. B*, 1976, **13**, 5188–5192.
23 S. Plimpton, *Journal of Computational Physics*, 1995, **117**, 1 – 19.
24 D. Raymand, A. C. van Duin, M. Baudin and K. Hermansson, *Surface Science*, 2008, **602**, 1020 – 1031.
25 D. Raymand, A. C. van Duin, D. Spångberg, W. A. G. III and K. Hermansson, *Surface Science*, 2010, **604**, 741 – 752.
26 S. A. P. A. Y. G. H. M. Aktulga, J. C. Fogarty, *Parallel Computing*, 2012, **38**, 245–259.
27 G. Henkelman and H. Jónsson, *The Journal of Chemical Physics*, 2000, **113**, 9978–9985.
28 G. Henkelman, B. P. Uberuaga and H. Jónsson, *The Journal of Chemical Physics*, 2000, **113**, 9901–9904.
29 A. Nakano, *Computer Physics Communications*, 2008, **178**, 280 – 289.
30 E. H. Kisi and M. M. Elcombe, *Acta Crystallographica Section C*, 1989, **45**, 1867–1870.
31 U. of Rhode Island. Coastal Resources Center, *CRC handbook of chemistry and physics*, Cleveland, Ohio : CRC Press, 1978.
32 B. Meyer and D. Marx, *Phys. Rev. B*, 2003, **67**, 035403.
33 X. Shen, P. B. Allen, J. T. Muckerman, J. W. Davenport and J.-C. Zheng, *Nano Letters*, 2007, **7**, 2267–2271.
34 Z. Fu-Chun, Z. Zhi-Yong, Z. Wei-Hu, Y. Jun-Feng and Y. Jiang-Ni, *Chinese Physics B*, 2009, **18**, 2508.
35 K. Sarasamak, A. J. Kulkarni, M. Zhou and S. Limpijumnong, *Phys. Rev. B*, 2008, **77**, 024104.
36 A. Zaoui and W. Sekkal, *Phys. Rev. B*, 2002, **66**, 174106.
37 W.-J. Li, E.-W. Shi, W.-Z. Zhong and Z.-W. Yin, *Journal of Crystal Growth*, 1999, **203**, 186 – 196.
38 U. Diebold, L. V. Koplitz and O. Dulub, *Applied Surface Science*, 2004, **237**, 336 – 342.
39 C.-C. Röhlig, M. Niebelschütz, K. Brueckner, K. Tonisch, O. Ambacher and V. Cimalla, *physica status solidi (b)*, 2010, **247**, 2557–2570.
40 M. M. J. Treacy, T. W. Ebbesen and J. M. Gibson, *Nature*, 1996, **381**, 678–680.
41 R. Agrawal, B. Peng, E. E. Gdoutos and H. D. Espinosa, *Nano Letters*,

2008, **8**, 3668–3674.
42 G. N. Greaves, A. L. Greer, R. S. Lakes and T. Rouxel, *Nat Mater*, 2011, **10**, 823–837.
43 X. D. Bai, P. X. Gao, Z. L. Wang and E. G. Wang, *Applied Physics Letters*, 2003, **82**, 4806–4808.
44 K. Yum, Z. Wang, A. P. Suryavanshi and M.-F. Yu, *Journal of Applied Physics*, 2004, **96**, 3933–3938.
45 Y. Huang, X. Bai and Y. Zhang, *Journal of Physics: Condensed Matter*, 2006, **18**, L179.
46 H. Ni and X. Li, *Nanotechnology*, 2006, **17**, 3591.
47 J. Song, X. Wang, E. Riedo and Z. L. Wang, *Nano Letters*, 2005, **5**, 1954–1958.
48 M. P. Manoharan, A. V. Desai, G. Neely and M. A. Haque, *J. Nanomaterials*, 2008, **2008**, 49:1–49:7.
49 S. Hoffmann, F. Östlund, J. Michler, H. J. Fan, M. Zacharias, S. H. Christiansen and C. Ballif, *Nanotechnology*, 2007, **18**, 205503.
50 A. Desai and M. Haque, *Sensors and Actuators A: Physical*, 2007, **134**, 169 – 176.
51 C. Q. Chen, Y. Shi, Y. S. Zhang, J. Zhu and Y. J. Yan, *Physical Review Letters*, 2006, **96**, year.
52 J. Zhou, C. S. Lao, P. Gao, W. Mai, W. L. Hughes, S. Z. Deng, N. S. Xu and Z. L. Wang, *Solid State Communications*, 2006, **139**, 222 – 226.
53 B. Wen, J. E. Sader and J. J. Boland, *Phys. Rev. Lett.*, 2008, **101**, 175502.
54 L. W. Yang, X. L. Wu, T. Qiu, G. G. Siu and P. K. Chu, *Journal of Applied Physics*, 2006, **99**, 074303.
55 D. Jiang, C. Tian, Q. Liu, M. Zhao, J. Qin, J. Hou, S. Gao, Q. Liang and J. Zhao, *Materials Science and Engineering: A*, 2014, **610**, 1 – 4.
56 MultiMedia, *Staying Cool on the ISS*, 2001, `http://science.nasa.gov/science-news/science-at-nasa/2001/ast21mar_1/`.